Effects of microscopic transport coefficients on fission observables calculated by the Langevin equation

M. D. Usang*
Tokyo Institute of Technology, Tokyo, Japan
and Malaysian Nuclear Agency, Bangi, Malaysia

F. A. Ivanyuk
Tokyo Institute of Technology, Tokyo, Japan
and Institute for Nuclear Research, Kiev, Ukraine

C. Ishizuka
Tokyo Institute of Technology, Tokyo, Japan

S. Chiba
Tokyo Institute of Technology, Tokyo, Japan
and National Astronomical Observatory of Japan, Tokyo, Japan

(Received 3 June 2016; revised manuscript received 8 August 2016; published 7 October 2016)

Nuclear fission is treated by using the Langevin dynamical description with macroscopic and microscopic transport coefficients (mass and friction tensors), and it is elucidated how the microscopic (shell and pairing) effects in the transport coefficients, especially their dependence on temperature, affects various fission observables. We found that the microscopic transport coefficients, calculated by linear response theory, change drastically as a function of temperature: in general, the friction increases with growing temperature while the mass tensor decreases. This temperature dependence brings a noticeable change in the mass distribution and kinetic energies of fission fragments from nuclei around ^{236}U at an excitation energy of 20 MeV. The prescission kinetic energy decreases from 25 MeV at low temperature to about 2.5 MeV at high temperature. In contrast, the Coulomb kinetic energy increases as the temperature increases. Interpolating the microscopic transport coefficients among the various temperatures enabled our Langevin equation to use the microscopic transport coefficients at a deformation-dependent local temperature of the dynamical evolution. This allowed us to compare directly the fission observables of both macroscopic and microscopic calculations, and we found almost identical results under the conditions considered in this work.

DOI: 10.1103/PhysRevC.94.044602

I. INTRODUCTION

Nuclear fission continues to be an interesting subject from a basic research point of view, since it involves large-scale collective motion leading to violent rearrangement of nucleons, exhibiting a strong quantum nature (shell and pairing effects) in the low-energy region. Nuclear fission is also the basic phenomenon in many applications such as nuclear technology and medicine. There are many observables associated with fission: excitation function, angular distribution of fission fragments, mass and charge (or isotopic) distribution of fission fragments, their kinetic energies, pre- and post-fission particle emissions, and so on. All these observables are correlated to each other, and hence should be considered or treated in a consistent manner. This requires a deep understanding of nuclear fission.

Statistical approaches in terms of reproducing the results of fission observables have seen success [1–5], although most of them include phenomenology to a great extent, or the range of their applicability is limited. The dynamical studies of fission—typical reviews are given in Refs. [6,7]-have had a good measure of success in recent years in reproducing the results of experimental data. Comparison of dynamical results is often made for the mass yield distribution of fission fragments and the associated kinetic energy [8–13]. The attention given to the dynamical study of fission is due to possible insights it offered into our deeper understanding of fission phenomena with less phenomenology or assumption. For example, the role of shell effects is essential in fission at low excitation energy, with special attention given to the production of a double-humped shape of the mass and charge distributions of fission fragments. It has often been shown that by excluding shell effects, one will obtain a single-peak result. Shell effects [14,15] are introduced here by using a shell correction to the potential energy surface [11–13]. In the literature, one often encounters the use of mass and friction, which are referred to as "transport coefficients" in general, inspired from the macroscopic concepts for the calculation of the Langevin equation [10–13]. Most common is the use of hydrodynamical mass [16,17] and friction [18,19]. These "macroscopic" transport coefficients are used mainly because of the simplicity of calculating them in most of the previous works on fission. However, they do not contain any quantum

*usang.m.aa@m.titech.ac.jp; mark_dennis@nm.gov.my

effects even though it was found that, as explained above, quantum effects in the potential energy surface are essential to understand the double-humped structure of mass (or charge) distribution of fission fragments for low-energy fission of many actinides. Furthermore, the microscopic transport coefficients reveal strong temperature dependence, a feature which is completely missing in the macroscopic transport coefficients. The microscopic transport coefficients have been discussed in many textbooks and review articles; see, for example, [20–25]. However, up to now the microscopic mass and friction tensors were employed in the Langevin calculation of the fusion-fission (or quasifission) process only in works by the Omsk-Dubna-Kiev group [26,27]. The so-called diagonal component of the microscopic mass tensor was used in [28,29] for the description of fusion reactions within the concept of a dinuclear system.

In the present work, we seek to improve the current understanding of the fission process of actinides at lower excitation energy region, where quantum (shell and pairing) effects are essential, by introducing microscopic effects into the mass and friction as well as in the potential energy for use in the Langevin equation.

Incorporating microscopic effects into the mass and friction is done by means of linear response theory and local harmonic approximation [30]. Linear response theory is commonly used to analyze the response to external disturbances on the system. The application of the theory is wide ranging; the most obvious uses are in signal analysis and radio transducers. It extends almost to any system that we can describe as an oscillator. In quantum theory applications, the theory is introduced by Kubo [31] to describe the fluctuation and dissipation theorem in a many-particle system.

This paper is organized as follows. In Sec. II, we will describe how the nuclear shape and potentials are parametrized. In Sec. III, the way to calculate transport coefficients, both in macroscopic and microscopic models, is described, and typical results of both types of calculations are compared. In Sec. IV, we perform the Langevin calculation by using both types of transport coefficients, and discuss how the quantum effects, especially the temperature dependence of the microscopic transport coefficients, will affect various observables in nuclear fission. Section V is devoted to concluding remarks.

II. THE SHAPE PARAMETRIZATION AND THE POTENTIAL ENERGY

In present work we use the two-center shell model suggested by Maruhn and Greiner [32] and the code developed by Suekane, Iwamoto, Yamaji, and Harada [33,34]. In this model the mean-field potential includes the central part $V(\rho,z)$, **ls**, and $\mathbf{l}^2$ terms. The potential $V(\rho,z)$ in the two-center shell model consists of two oscillator potentials smoothly connected together (see Fig. 1),

$$V(\rho,z)=\begin{cases}\frac{1}{2}m\omega_{z_1}^2(z-z_1)^2+\frac{1}{2}m\omega_{\rho_1}^2\rho^2, & z\leqslant z_1,\\ \frac{1}{2}m\omega_{z_1}^2(z-z_1)^2 f_1(z,z_1)+\frac{1}{2}m\omega_{\rho_1}^2\rho^2 f_2(z,z_1) & z_1\leqslant z\leqslant 0,\\ \frac{1}{2}m\omega_{z_2}^2(z-z_2)^2 f_1(z,z_2)+\frac{1}{2}m\omega_{\rho_2}^2\rho^2 f_2(z,z_2) & 0\leqslant z\leqslant z_2,\\ \frac{1}{2}m\omega_{z_2}^2(z-z_2)^2+\frac{1}{2}m\omega_{\rho_2}^2\rho^2, & z_2\leqslant z,\end{cases} \tag{1}$$

with

$$\begin{aligned} f_1(z,z_i)&=1+c_i(z-z_i)+d_i(z-z_i)^2,\\ f_2(z,z_2)&=1+g_i(z-z_i)^2.\end{aligned} \tag{2}$$

The potential (1)–(2) contains 12 parameters. By imposing conditions that parts of the potential are joined smoothly at $z=z_1, z=z_2$, and $z=0$, the number of parameters is reduced to 5. These are the elongation parameter $z_0\equiv z_2-z_1$, the mass asymmetry $\alpha=(V_1-V_2)/(V_1+V_2)$ (V_1 and V_2 are the volumes to the left and right from $z=0$), the deformations δ_i of the left and right oscillator potentials, and the neck parameter ϵ. The neck parameter ϵ is given by the ratio of the potential height E at $z=0$ to the value E_0 of left and right harmonic oscillator potentials at $z=0$ (which should be the same); see Fig 1. All the parameters appearing in (1) can be expressed in terms of these five deformation parameters.

The ratio of oscillator frequencies ω_ρ/ω_z or the ratio of semi-axes in ρ and z directions is related to the deformation parameters δ_i as

$$\frac{\omega_{\rho i}}{\omega_{zi}}\equiv B_i=\frac{3+\delta_i}{3-2\delta_i}. \tag{3}$$

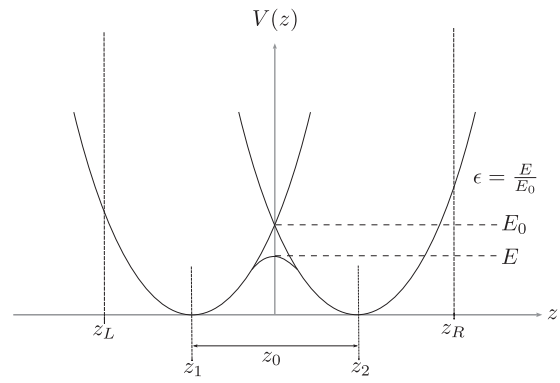

FIG. 1. The two-center shell model potential (1) for $\rho=0$.

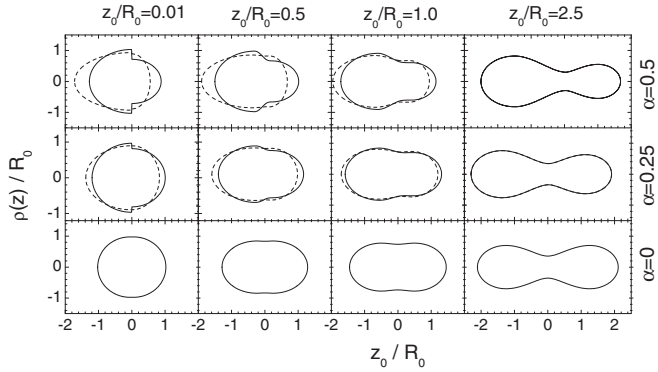

FIG. 2. The shape of a nuclear surface calculated with the two-center shell model parametrization ($\delta = 0.2$, $\epsilon = 0.35$, solid lines) and the modification (6) (dashed lines).

The shape of the nuclear surface within TCSM is identified with the surface of constant potential (1), $V(\rho(z),z) = V_0$. The constant V_0 is found from the requirement that the volume inside the equipotential surface is equal to the volume of a spherical nucleus.

Few examples of the profile function $\rho(z)$ are shown in Fig. 2 (solid curves). In the left part of the figure one sees the well known drawback of the restricted ($\delta_1 = \delta_2 \equiv \delta$) two-center shell model shape parametrization: for $z_0 = 0$ the profile function is discontinuous for $\alpha \neq 0$. This difficulty can be overcome imposing the condition

$$\rho(z = z_1) = \rho(z = z_2). \tag{4}$$

From the definition of the profile function $\rho(z)$ it can be shown in a formal way that condition (4) is fulfilled if $B_1/B_2 = (1+\alpha)/(1-\alpha)$. The last relation offers the introduction of the α-dependent deformation parameters B_1 and B_2,

$$\begin{aligned} B_1(\delta,\alpha) &= B_0(1+\alpha), \\ B_2(\delta,\alpha) &= B_0(1-\alpha), \\ \text{with} \quad B_0 &= (3+\delta)/(3-2\delta). \end{aligned} \tag{5}$$

It is clear that condition (4) should hold true only for small values of z_0. At large values of z_0 the profile function $\rho(z)$ is quite smooth and B_1, B_2 should turn into B_0 (in the case that $\delta_1 = \delta_2$). This is achieved by introducing a weighting function $f(z_0)$ that guaranties the smooth transition from B_1, B_2 to B_0 as z_0 becomes large:

$$\begin{aligned} B_1(\delta,\alpha) &= f(z_0)B_0(1+\alpha) + [1-f(z_0)]B_0, \\ B_2(\delta,\alpha) &= f(z_0)B_0(1-\alpha) + [1-f(z_0)]B_0, \end{aligned} \tag{6}$$

with

$$f(z_0) = 1/\{1 + \exp[(z_0 - z_{00})/\Delta z_0]\}. \tag{7}$$

The parameters z_{00} and Δz_0 are fixed in the present work as $z_{00} = R_0$ and $\Delta z_0 = 0.2R_0$. So, the factor $f(z_0)$ is close to 1 at small values of z_0 and is negligibly small for large values of z_0. As one can see from Fig. 2 the discontinuity of the profile function $\rho(z)$ at small values of z_0 disappears.

The potential energy surface is one of the most important ingredients of the Langevin equation. At low excitation energy the collective motion is slow and the dynamical trajectories follow mainly the bottom of the potential energy valley. Looking at the potential energy, one can estimate roughly the most probably masses of the fission fragments.

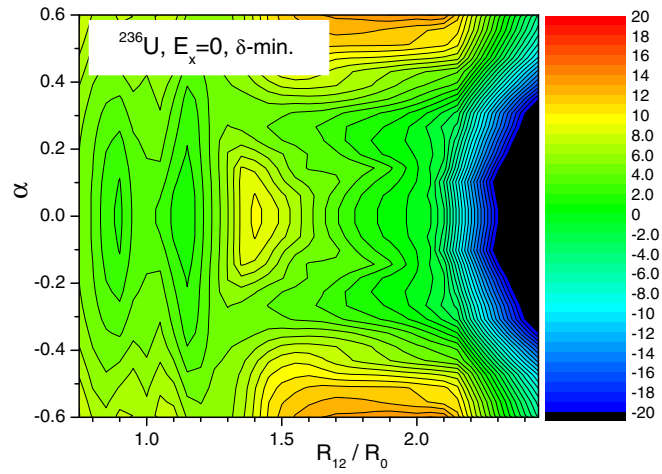

FIG. 3. The deformation energy of ^{236}U as function of elongation (the distance R_{12} between the centers of mass of left and right parts of the nucleus) and the mass asymmetry α.

As in [35], in the present work we calculate the potential energy within the macroscopic-microscopic method [20,36,37]. In this method the deformation energy is represented as the sum of the macroscopic part $E_{\rm def}^{\rm LD}$ and the shell correction δE (including the shell correction to the pairing energy):

$$E_{\rm def} = E_{\rm def}^{\rm LD} + \delta E \quad \text{with } \delta E = \sum_{n,p} \left(\delta E_{\rm shell}^{(n,p)} + \delta E_{\rm pair}^{(n,p)}\right). \tag{8}$$

The summation in (8) is carried out over the protons (p) and neutrons (n). The $E_{\rm def}^{\rm LD}$ in (8) is the macroscopic part of the deformation energy, $E_{\rm def}^{\rm LD} = E_{\rm LD} - E_{\rm LD}^{\rm (sph)}$. The $E_{\rm LD}$ was calculated with the finite-range liquid drop model [38] as the sum of the surface energy $E_{\rm S}$ and the Coulomb energy $E_{\rm C}$, and $E_{\rm LD}^{\rm (sph)}$ is the liquid-drop energy for spherical shape.

The $\delta E_{\rm shell}$ was calculated from the single-particle levels of the two-center shell model potential [32–34] as the difference between the sum of single-particle energies of occupied states and the averaged quantity. The pairing correlation energy $E_{\rm pair}$ was evaluated in the BCS approximation following [20].

The calculated deformation energy $E_{\rm def}$ (8) of the nucleus ^{236}U is shown in Fig. 3 as function of elongation R_{12} (the spherical shape corresponds to $R_{12} = 0.75R_0$) and the mass asymmetry α. The energy was minimized with respect to the deformation of fragments ($\delta_1 = \delta_2 = \delta$) keeping fixed R_{12} and α. One can clearly see the ground state, the mass-asymmetric saddle, and the scission region.

III. TRANSPORT COEFFICIENTS FOR SLOW COLLECTIVE MOTION

A. Macroscopic friction and mass parameters

The Langevin equations are often solved with the so-called macroscopic transport coefficients. The macroscopic

mass tensor $M^{WW}_{\mu\nu}$ is usually defined in the Werner-Wheeler approximation [16]

$$M^{WW}_{\mu\nu} = \pi\rho_0 \int \rho^2(z)\left[A_\mu(z)A_\nu(z) + \frac{\rho^2(z)}{8}A'_\mu(z)A'_\nu(z)\right]dz, \tag{9}$$

with

$$A_\mu(z;Q) = \frac{1}{\rho^2(z,Q)}\frac{\partial}{\partial Q_\mu}\int_z^{z_{\max}} \rho^2(z',Q)dz'. \tag{10}$$

The popular expression for the macroscopic friction is the so called wall formula for friction [19]. According to [19], friction coefficient $\gamma^{\rm wall}$ is proportional to the squared normal velocity $u_n^2(s)$ of the surface, integrated over the nuclear surface. Following [19] this may be deduced from the loss of collective energy, which is given by

$$\dot{E} = \frac{3}{4}\rho_0 v_F \oint u_n^2(s)ds = \sum_{\mu\nu}\gamma^{\rm wall}_{\mu\nu}\dot{q}_\mu\dot{q}_\nu, \tag{11}$$

where v_F and ρ_0 are the Fermi velocity and the nucleon density, $\rho_0 = A/(4\pi R_0^3/3)$. For axial symmetric shapes the surface velocity $u_n(s)$ can be expressed in terms of derivatives of the profile function $\rho(z;Q)$, and the wall friction coefficient turns into

$$\gamma^{\rm wall}_{\mu\nu} = \frac{3\pi}{4}\rho_0 v_F \int \frac{\partial\rho^2}{\partial Q_\mu}\frac{\partial\rho^2}{\partial Q_\nu}\left[4\rho^2 + \left(\frac{\partial\rho^2}{\partial z}\right)^2\right]^{-1/2}dz. \tag{12}$$

The expression (12) was derived for a semi-infinite system, so for the Fermi momentum $\hbar k_F = m v_F$ we use here the estimate from the infinite Fermi gas, $k_F R_0 = (9\pi A/4)^{1/3}$.

From the derivation of the wall formula it is clear that u_n is the velocity of the surface with respect to the bulk of the gas. When applied to a rotating or translating nucleus u_n has to be measured with respect to a comoving or corotating frame. For configurations close to scission it seems natural to associate the average velocity of particles in each of the two fragments with the center-of-mass velocity of the fragment. The friction tensor then becomes [39] (see also [23])

$$\gamma^{\rm wall\,2}_{\mu\nu} = \frac{3\pi}{4}\rho_0 v_F\left(\int_{z_{\min}}^{0} I_L(z)dz + \int_0^{z_{\max}} I_R(z)dz\right), \tag{13}$$

with

$$I_{L,R}(z) = \left(\frac{\partial\rho^2}{\partial Q_\mu} + \frac{\partial\rho^2}{\partial z}\frac{\partial z_{cm}(L,R)}{\partial Q_\mu}\right) \times \left(\frac{\partial\rho^2}{\partial Q_\nu} + \frac{\partial\rho^2}{\partial z}\frac{\partial z_{cm}(L,R)}{\partial Q_\nu}\right)\left[4\rho^2 + \left(\frac{\partial\rho^2}{\partial z}\right)^2\right]^{-1/2}. \tag{14}$$

It was also suggested [40] that close to scission the wall friction should be corrected by the "window term"

$$\gamma^{\rm window}_{\mu\nu} = \frac{1}{2}\rho_0\bar{v}\left[\Delta\sigma\left(\frac{\partial R_{12}}{\partial Q_\mu}\frac{\partial R_{12}}{\partial Q_\nu}\right) + \frac{32}{9\Delta\sigma}\frac{\partial V_L}{\partial Q_\mu}\frac{\partial V_L}{\partial Q_\nu}\right], \tag{15}$$

so that the "wall friction" turns into "wall-and-window" friction tensor

$$\gamma^{w+w}_{\mu\nu} = \gamma^{\rm wall\,2}_{\mu\nu} + \gamma^{\rm window}_{\mu\nu}. \tag{16}$$

One expects a smooth transition between the regime in which the wall formula applies and the part of fission path where wall-and-window friction should be used. For this Nix and Sierk [41] proposed the phenomenological ansatz

$$\gamma^{\rm total}_{\mu\nu} = \sin^2(\pi\alpha/2)\gamma^{\rm wall}_{\mu\nu} + \cos^2(\pi\alpha/2)\gamma^{w+w}_{\mu\nu}, \tag{17}$$

with $\alpha = (r_{\rm neck}/R_{\min})^2$, where $R_{\min}$ is the minimal semi-axis of two outer ellipsoids in three-quadratic-surfaces shape parametrization.

Equations (9) and (12) provide rather simple expressions for the tensors of frictions and inertia. The macroscopic transport coefficients depend only on the shape (deformation) of the system. They do not contain any quantum effects which should be important at least at low excitation energies.

B. Microscopic friction and mass parameters

The so-called microscopic transport coefficients can be defined within the linear response approach and the local harmonic approximation [30]. This approach is based on the microscopic nuclear Hamiltonian. Thus, many quantum effects, such as the shell and pairing effects and the dependence of the collisional width of single-particle states on the excitation energy, are taken into account. The two main ingredients of this approach are the mean-field Hamiltonian and the account of the collisional width of single-particle states. For the mean-field Hamiltonian we use here the two-center shell model. For the collisional width of single-particle states in the presence of pairing effects we use the expression derived in [42].

The precise expressions for the friction $\gamma_{\mu\nu}$ and mass tensors $M_{\mu\nu}$ one can find in [43]. These are

$$\gamma_{\mu\nu}(0) = 2\hbar{\sum_{jk}}'\left(n_k^T - n_j^T\right)\xi_{kj}^2\frac{E_{kj}^-\Gamma_{kj}}{\left[(E_{kj}^-)^2 + \Gamma_{kj}^2\right]^2}F_\mu^{kj}F_\nu^{jk} + 2\hbar\sum_{jk}\left(n_k^T + n_j^T - 1\right)\eta_{kj}^2\frac{E_{kj}^+\Gamma_{kj}}{\left[(E_{kj}^+)^2 + \Gamma_{kj}^2\right]^2}F_\mu^{kj}F_\nu^{jk}, \tag{18}$$

$$M_{\mu\nu}(0) = \hbar^2{\sum_{jk}}'\left(n_k^T - n_j^T\right)\xi_{kj}^2\frac{E_{kj}^{-2}[E_{kj}^- - 3\Gamma_{kj}]}{\left[(E_{kj}^-)^2 + \Gamma_{kj}^2\right]^3}F_\mu^{kj}F_\nu^{jk} + \hbar^2\sum_{jk}\left(n_k^T + n_j^T - 1\right)\eta_{kj}^2\frac{E_{kj}^{+2}[E_{kj}^+ - 3\Gamma_{kj}]}{\left[(E_{kj}^+)^2 + \Gamma_{kj}^2\right]^3}F_\mu^{kj}F_\nu^{jk}. \tag{19}$$

Here E_k, E_j are the energies of quasiparticle states in the BCS approximation, $E_{kj}^- \equiv E_k - E_j$, $E_{kj}^+ \equiv E_k + E_j$, $n_k^T \equiv 1/[1+\exp(E_k/T)]$, $\eta_{kj} = u_k\upsilon_j + u_j\upsilon_k$, $\xi_{kj} = u_k u_j - \upsilon_k\upsilon_j$, and u_k, υ_k are the coefficients of Bogoliubov-Valatin transformation. The operator $\hat{F}_\mu$, which appears in (18)–(19), is the derivative of the single-particle Hamiltonian with respect to the deformation parameter Q_μ. The quantity Γ_{kj} is the average

width of the two-quasiparticle states, $\Gamma_{kj} = [\Gamma(E_k,\Delta,T) + \Gamma(E_j,\Delta,T)]/2$. The calculation of Γ_{kj} for the system with pairing is explained in detail in [42].

In (18)–(19) the summation is carried out over the single-particle states $|k\rangle$ and $|l\rangle$. More precisely, the contributions to the first sums in (18)–(19) come only from the nondiagonal matrix elements F_μ^{kj}. The first sums are different from zero only for $T \neq 0$ (for $T = 0$ all n_k^T are equal to zero). The second sums in (18)–(19) are finite also in case $T = 0$. Both diagonal and nondiagonal matrix elements F_μ^{kj} contribute to these sums.

As in the case of the cranking mass parameter calculated within the BCS approximation, the diagonal contribution to (19) is proportional to $1/\Delta^2$; see [20]. So, at the deformation points where the density of single-particle states at the Fermi energy is very small, or close to the critical temperature where the pairing gap disappears, the the diagonal contribution to (19) becomes unreasonably large. Luckily, at the same deformation point the friction tensor is large too for the same reason. The quantity that is essential for the Langevin equations is the ratio $\gamma_{\mu\nu}/M_{\mu\nu}$. This ratio is a much smoother function of deformation compared to both $\gamma_{\mu\nu}$ and $M_{\mu\nu}$. So, large diagonal contributions to $\gamma_{\mu\nu}$ and $M_{\mu\nu}$ do not cause many problems in solving the Langevin equations.

The expressions (18)–(19) were derived within the quantum approach with the shell and pairing effects taking into account. In what follows we will call these expressions *microscopic transport coefficient*s.

C. Numerical results for the transport coefficients

A comparison of the z_0z_0 component of microscopic transport coefficients calculated for several values of temperature $T_{\rm tr}$ is shown in Fig. 4. Here, the quantity $T_{\rm tr}$ is referred to as the *microscopic transport temperature* and denotes the thermodynamical temperature at which the microscopic transport coefficients are calculated.

Like in the previous calculation [35,42] the deformation dependence of both friction and mass tensors shows sharp peaks at avoided crossings of single-particle energies close to the Fermi energy. For several reasons it was claimed in [42] that to a large extent such fluctuations are shortcomings of the underlying shell model. It was suggested to overcome these difficulties by averaging the transport coefficients over deformation. The averaging interval should be large enough to smooth out the rapid oscillations, as well as the fine details of the shell structure, but at the same time small enough to preserve gross shell effects. The microscopic friction and mass tensors (18)–(19) shown in Fig. 4 were averaged in elongation z_0 on the interval $\Delta z_0 = 0.1R_0$. The averaging procedure is described in detail in [35].

As we can see from Fig. 4, the microscopic mass tensor decreases with increasing $T_{\rm tr}$ while the friction tensor increases as $T_{\rm tr}$ increases. At large temperatures both microscopic friction and mass coefficients look similar to macroscopic friction and mass. At small temperatures the microscopic and macroscopic transport coefficients deviate from each other very much. Thus, the results of dynamical calculations with the microscopic and macroscopic transport coefficients can deviate from each other

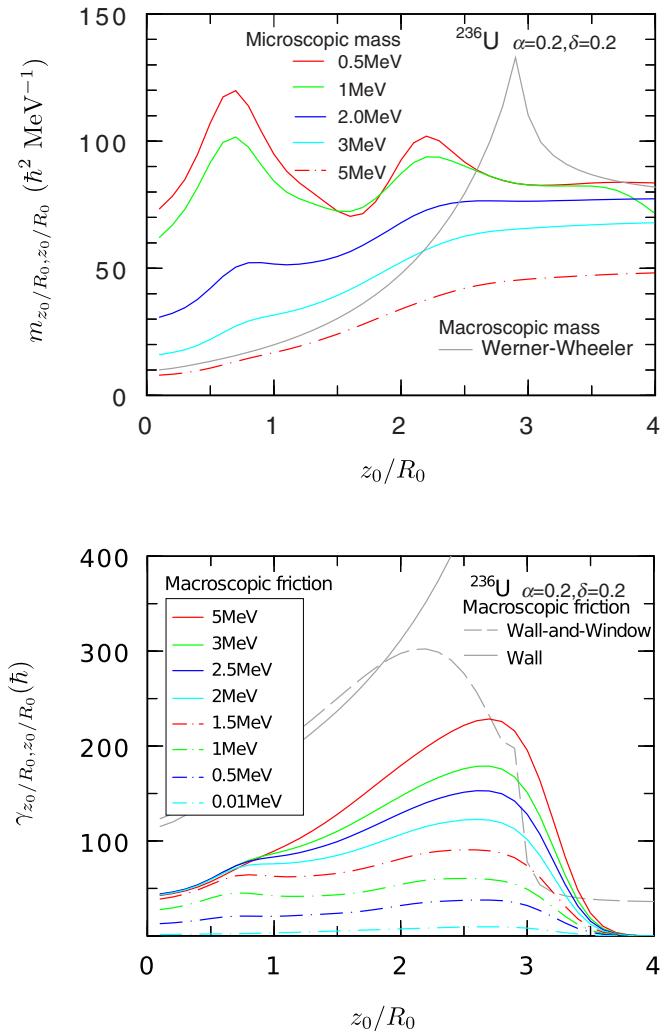

FIG. 4. Comparison of the z_0z_0 component of the microscopic mass tensor (19) calculated at several values of $T_{\rm tr}$ with the Werner-Wheeler approximation (9) (top) and a similar comparison of the z_0z_0 component of the microscopic friction tensor (18) for several values of $T_{\rm tr}$ with the macroscopic approximation (17) (bottom).

at, e.g., the saddle, where the temperature can be quite small. The comparison of the microscopic and macroscopic transport coefficients calculated within the two-center shell model shape parametrization can be found also in [35].

The components of the mass tensor (19) calculated for the typical temperature $T = 1$ MeV and fixed $\delta = 0.2$ are shown as function of elongation z_0/R_0 and mass asymmetry α in Fig. 5. It turns out that the diagonal and nondiagonal components of the mass tensor do not differ much in magnitude. That means that equations for the time variation of deformation parameters in (20) are strongly coupled to each other. All three parameters change at more or less the same speed. One can not say that, for example, the motion in z_0/R_0 is fast and motion in δ is slow.

The frequency of fluctuations in the deformation dependence of the mass tensor is approximately the same as in the case of potential energy. So, these fluctuations can be related to the shell structure. It is difficult, however, to say what is

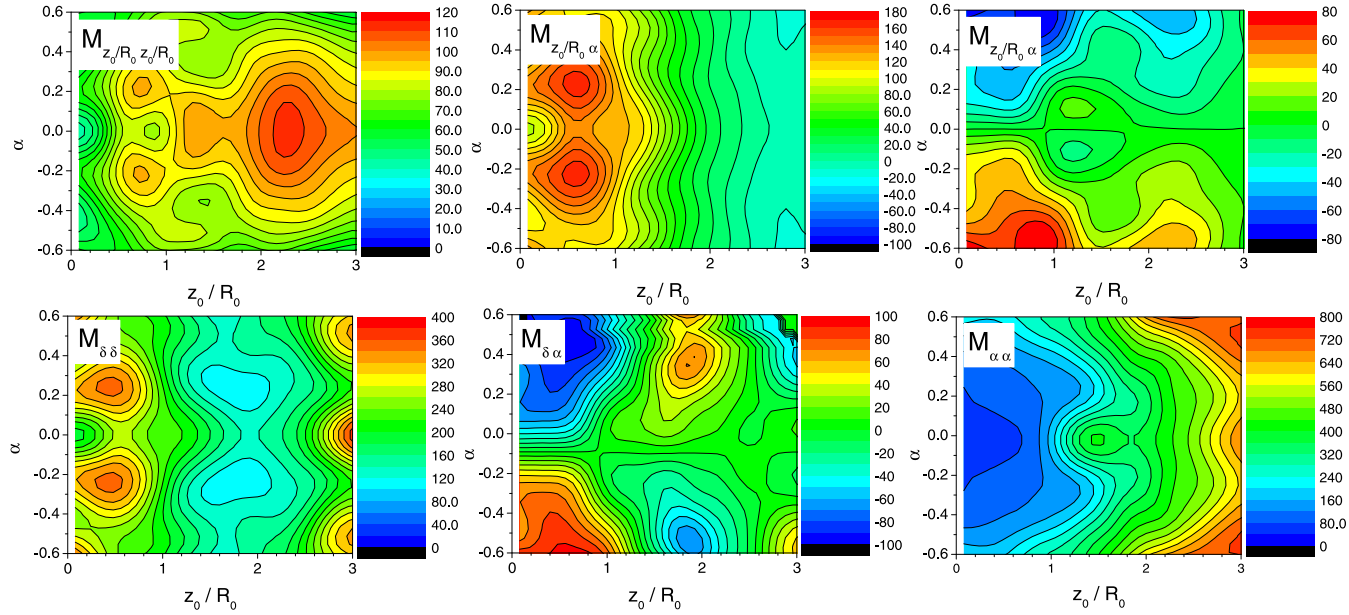

FIG. 5. The components of the microscopic mass tensor (19) calculated for $\delta = 0.2$ and $T = 1$ MeV.

the effect of these fluctuations on the fission observables. Many trajectories in the multidimensional deformation space contribute to the final results and the effects of fluctuations should be averaged somehow.

At $T = 1$ MeV all components of mass tensor (19) are several times larger that these calculated within the Werner-Wheeler approximation. So, in principle, the macroscopic and microscopic descriptions of the fission process can lead to different results.

IV. LANGEVIN EQUATION

The Langevin equation for the description of fissioning nuclei are defined as a system of first-order differential equations,

$$\begin{aligned}\frac{dq_\mu}{dt} &= (m^{-1})_{\mu\nu}p_\nu \\ \frac{dp_\mu}{dt} &= -\frac{\partial V}{\partial q_\mu} - \frac{1}{2}\frac{\partial}{\partial q_\mu}(m^{-1})_{\nu\sigma}p_\nu p_\sigma \\ &\quad - \gamma_{\mu\nu}(m^{-1})_{\nu\sigma}p_\sigma + g_{\mu\nu}R_\nu(t),\end{aligned} \tag{20}$$

where the collective coordinates, $\{q_i\} = (z_0/R_0, \delta, \alpha)$ were introduced in the previous section. As a brief reminder, z_0 is the elongation of the nucleus, R_0 is the radius of the spherical compound nucleus, δ is the deformation of fragments, and α is the mass asymmetry. The parameters δ_1 and δ_2 are assumed to be the same, $\delta_1 = \delta_2 = \delta$, and the neck parameter is kept constant, $\epsilon = 0.35$.

The smaller number of dynamical variables allows one to reduce the computation time to a manageable level. Here, as in the previous works, we use the value $\epsilon = 0.35$, which was recommended in Ref. [44] for the fission process. Keeping ϵ fixed does not mean that the neck radius is fixed. The neck radius within the two-center shell model shape parametrization depends on all five deformation parameters.

Even keeping the neck parameter ϵ fixed one gets a quite reasonable variety of fission shapes from the sphere to the two separated fragments; see Fig. 10 of [11]. The deformation energy calculated with $\epsilon = 0.35$ is rather close the that obtained with the optimal shapes [45]. Keeping ϵ fixed in dynamical calculations means that the neck radius is assumed to adjust itself infinitely fast to the equilibrium value defined by the other deformation parameters. Eventually, all the results obtained in the present work and previous dynamical calculations with constant ϵ confirm that fixed ϵ is quite a meaningful approximation for the fission process.

The momentum conjugate to each of the collective coordinates is denoted as p_μ. The symbol $(m^{-1})_{\mu\nu}$ denotes the inverse of mass tensor, and $\gamma_{\mu\nu}$ is the friction tensor.

The Langevin random force $g_{\mu\nu}R_\nu(t)$ is the product of white noise $R_\nu(t)$ and the temperature-dependent strength factors $g_{\mu\nu}$. The factors $g_{\mu\nu}$ are related to the temperature and friction tensor via the Einstein relation,

$$\sum_\sigma g_{\mu\sigma}g_{\sigma\nu} = T\gamma_{\mu\nu}. \tag{21}$$

The temperature, T in this context is related to the excitation energy E_x and internal energy $E_{\rm int}$,

$$E_{\rm int} = E_x - \tfrac{1}{2}(m^{-1})_{\mu\nu}p_\mu p_\nu - V(q, E_{\rm int}) = aT^2, \tag{22}$$

where a is the level density parameter. The temperature defined in this way will be referred to as "local temperature" in the following. The potential, $V(q)$ used here was calculated by the two-center shell model. The shell corrections $\delta E_{\rm shell}$ and $\delta E_{\rm pair}$, see (8), were calculated for $T = 0$. We account for the temperature dependence of the shell and pairing effects as

$$V(q, E_{\rm int}) = E^{\rm LD}_{\rm def} + \Phi_{\rm sh}(E_{\rm int})\delta E_{\rm shell} + \Phi_{\rm pair}(E_{\rm int})\delta E_{\rm pair}\,. \tag{23}$$

We adopted functions for the temperature dependence of shell and pair corrections described by Randrup and Möller [14]:

$$\Phi(E_{\rm int})_{\rm sh,pair} = \frac{1 + e^{E_1/E_0}}{e^{E_{\rm int}/E_0} + e^{E_1/E_0}}. \quad (24)$$

This form can be reduced to the description of Ignatyuk [15] by setting $e^{E_1/E_0} = 0$. The parameter E_0 is interpreted as the shell damping energy, and E_1 as an energy shift, as explained in Ref. [14].

The mass tensor $m_{\mu\nu}$ and friction tensor $\gamma_{\mu\nu}$ used in the Langevin equations were calculated both by macroscopic and microscopic models. In the macroscopic models, the mass tensor was calculated by the Werner-Wheeler approximation (9), and the friction tensor by a modified wall-and-window formula (17). In the microscopic calculation, the mass tensor $m_{\mu\nu}$ is calculated within the linear response theory (19). Similarly, the microscopic friction tensor is given by Eq. (18).

The Langevin calculation was started at either the potential minimum (the ground state) or around the second minimum. As far as the results presented in this work are concerned, both choices gave identical results. Initially, the momentum p_μ's were set to be zero, and Langevin motions were initiated by the conservative and random forces. Such calculations were continued until the trajectories reached scission points, which are defined as points where the neck radius becomes zero. Calculations were repeated typically 10^5 to 10^6 times, then final phase-space data were stored on a disk, and various quantities were calculated after all the Langevin calculations were finished.

V. FISSION PRODUCT YIELD

A. Macroscopic results

We describe in this paper the fission of the compound nucleus ^{236}U at the excitation $E_x = 20$ MeV and compare the calculated results with JENDL/FPY-2011 data [46] for 14 MeV neutron induced fission of ^{235}U. Prior to using microscopic calculations, we verified our code by using the macroscopic transport coefficients (see Fig. 6). All macroscopic results are calculated with $(E_0, E_1) = (15\ \text{MeV}, 30\ \text{MeV})$ in (24) for the damping of shell and pair corrections with increasing excitation energy.

The averages of mass yields for light and heavy fission fragments, which we denote as $\langle A_L \rangle$ and $\langle A_H \rangle$ henceforth, respectively are 94.4 and 135.2 each for the JENDL data. In our macroscopic calculation we obtained $\langle A_L \rangle = 96.7$ and $\langle A_H \rangle = 135.3$. As we can see, the agreement of the calculated mass yield and JENDL evaluated mass yield is reasonably good.

We have also calculated the mass yield with macroscopic transport coefficients including effects of multichance fission. For this purpose, we superposed mass distributions from ^{236}U, ^{235}U, and ^{234}U with fission probabilities calculated by GEF code [5] by successively reducing excitation energy, and obtained the multichance fission product yield as shown in Fig. 7. The multichance fission product yield shows aresult very similar to a pure first-chance result for the mass yield,

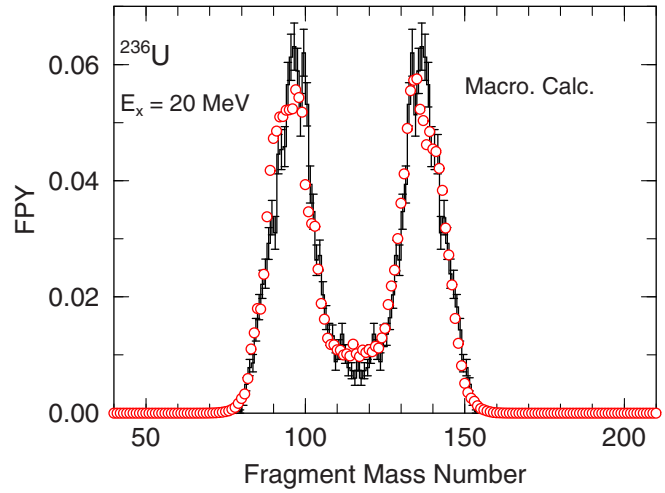

FIG. 6. The fission product yield (FPY) of ^{236}U at the excitation energy $E_x = 20$ MeV. The circles denote the experimental data from the library JENDL/FPY-2011 [46], while the present results obtained by using macroscopic transport coefficients are shown as a histogram. The error bars mark the statistical uncertainty of present results. The yield is normalized to 2.

and the averages for light and heavy mass fission fragments are $\langle A_L \rangle = 94.8$ and $\langle A_H \rangle = 136.3$, respectively. The largest change may be a slight reduction of the symmetric component, due to contributions of fission channels with reduced excitation energy. We expect that further adjustment of shell corrections could improve the current results, but still we can conclude that the multichance fission does not alter the main characteristics of the fission observables in the current condition. Therefore, all the results to be shown in the following were obtained as results of the calculation corresponding to the first-chance fission.

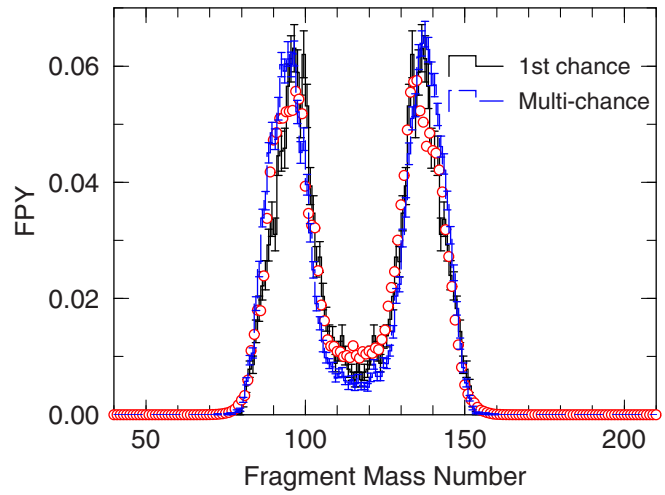

FIG. 7. The comparison of fission product yield of the multichance fission calculation (blue histogram), the first-chance fission calculation (black histogram), and JENDL data (red circles). The calculations were performed with the macroscopic transport coefficients.

B. Microscopic results

Contrary to the macroscopic results, all microscopic results are calculated with full shell correction, namely, $\Phi_{\mathrm{sh,pair}} = 1$. This is because we can adjust the combination of the shell correction parameters (E_0, E_1) to reproduce the experimental mass yields in various ways as shown in Ref. [14]. In this subsection, we would like to clarify the effect of microscopic transport coefficients by excluding ambiguities due to shell correction.

By using microscopic transport coefficients, we have to adjust them to the local temperature T defined in Eq. (22) as fission evolves.

By interpolating the microscopic transport coefficients calculated at several microscopic transport temperature, we can determine the microscopic transport coefficients at the local temperature given at each deformation; i.e., defining the temperature according to Eq. (22). We call such a calculation the microscopic local temperature calculation. In Fig. 8 we show the mass distribution obtained with microscopic local temperature including temperature-dependent microscopic effects on transport coefficients in the Langevin equation. We notice that the overall agreement with the data given JENDL/FPY-2011 is very close to what we got with macroscopic transport coefficients.

Similar calculations were performed for compound nuclei ^{234}U and ^{240}Pu at an excitation energy of 20 MeV, and are compared in Figs. 9 with data given in JENDL-4, which correspond respectively to ^{233}U $+n$ and ^{239}Pu $+n$ reactions at a neutron energy of 14 MeV. The agreement with the data given in JENDL-4 is almost equivalent to that of ^{236}U shown in Figs. 6 and 8; namely, both the calculations with macroscopic transport coefficients, which are independent of temperature, and that with microscopic transport coefficients, which depends on local temperature, can reproduce experimental information given in JENDL-4.

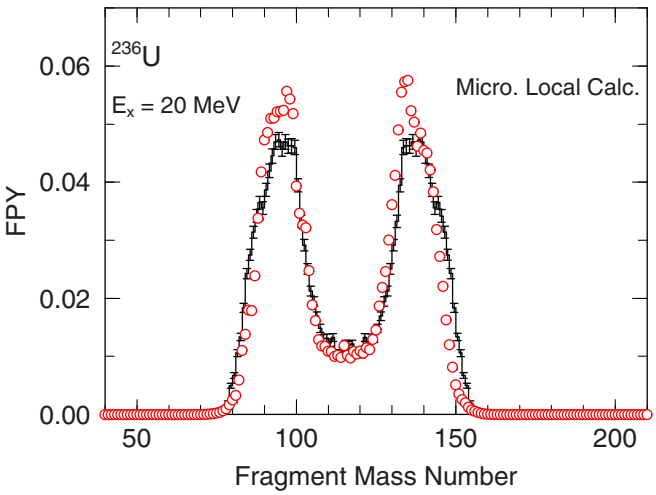

FIG. 8. The fission product yield for the ^{236}U compound nucleus at an excitation energy of 20 MeV calculated with the microscopic transport coefficients, which depend on deformation-dependent local temperature.

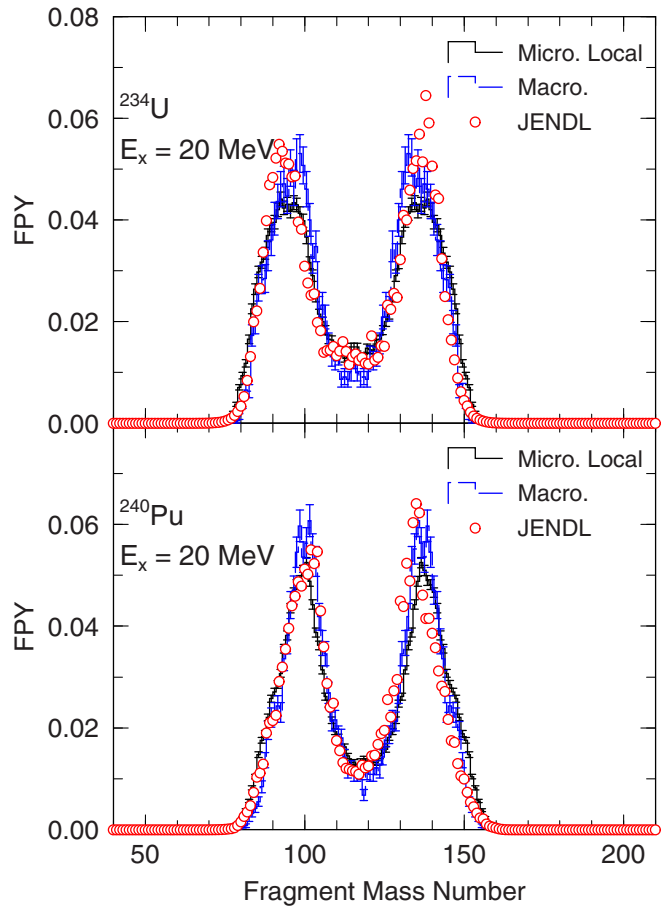

FIG. 9. The fission product yield for ^{234}U (top) and ^{240}Pu (bottom) compound nuclei at an excitation energy of 20 MeV calculated with the temperature-independent macroscopic (broken blue histogram) and microscopic (black histogram) transport coefficients at deformation-dependent local temperature compared with data given in JENDL-4 (red circles).

It is frequently argued that the pairing effect damps much faster than the shell effect. We have set the damping energy for the pairing effect to 5, 10, 20, 30 MeV and also set $\Phi_{\mathrm{pair}} = 1$ while keeping the shell correction factor Φ_{sh}, and compared mass distributions for ^{236}U in Fig. 10 for macroscopic (top) and deformation-dependent microscopic (bottom) transport coefficients. We can see that the change brought by different pairing correction factors is not significant. There seems to be a slight difference of sensitivity to the different choices of pairing correction between the results with macroscopic and microscopic transport coefficients in the symmetric component. However, the difference is well within the range of statistical uncertainty. Therefore, we can conclude that the pairing effect to the potential energy does not affect the mass distribution of the fission fragments noticeably in this fissioning nuclei region and excitation energy region.

VI. KINETIC ENERGY OF FISSION FRAGMENTS

Apart from the mass yields, additional important results are the prescission kinetic energy of fission fragments, Coulomb

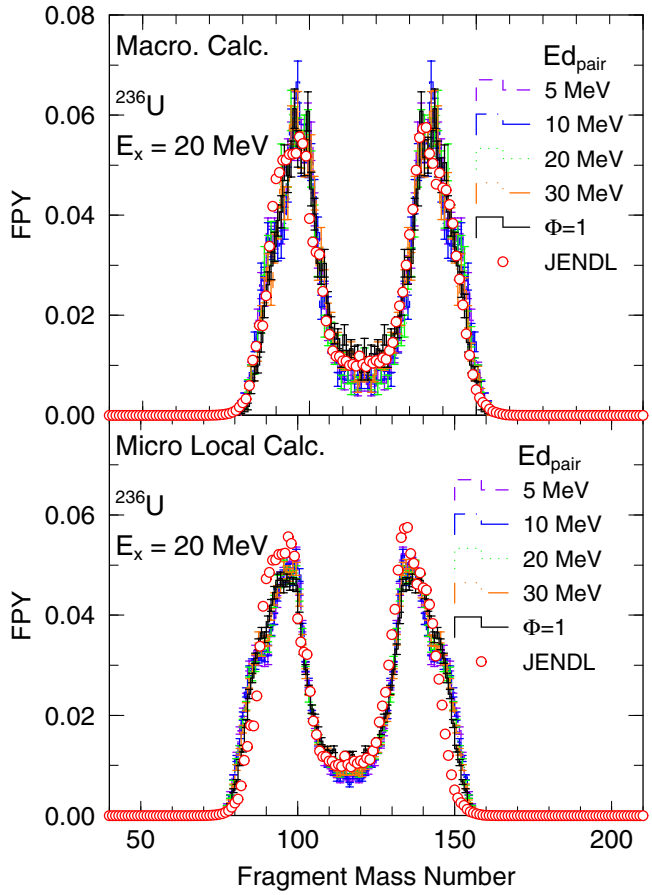

FIG. 10. The fission product yield for ^{236}U at an excitation energy of 20 MeV. The top figure compares the Langevin calculation with different choices of pairing correction energy (or factor) to the potential energy with macroscopic transport coefficients, while the bottom figure compares those calculated with microscopic transport coefficients, which depends on deformation-dependent local temperature.

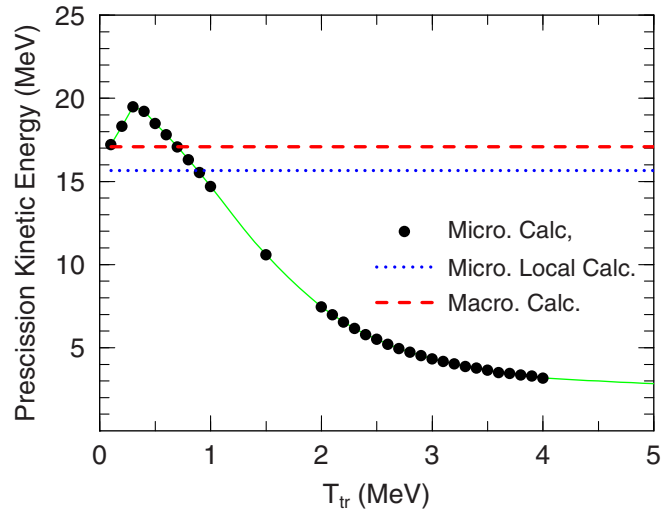

FIG. 11. The prescission kinetic energy of fission fragments as a function of temperature T_{tr} at which the transport coefficients were calculated for ^{236}U at $E_x = 20$ MeV. The horizontal red and blue lines denote the values calculated with the macroscopic transport coefficients and the local-temperature-dependent microscopic transport coefficients, respectively.

repulsion energy, and total kinetic energy. All the following calculations were performed for the compound ^{236}U nucleus at an excitation energy E_x of 20 MeV.

As the nuclide evolves from saddle to scission, a portion of the excitation energy of the system is transformed into the prescission kinetic energy of fragments. The dependence of prescission kinetic energy on the microscopic transport temperature T_{tr} is shown in Fig. 11 by circles connected by a solid line. Except for a region of very low T_{tr}, the prescission kinetic energy has generally a decreasing trend. This could be easily understood. As T_{tr} gets larger so does the friction tensor, which suppresses the kinetic energy acquired by fragments when they proceed to descend from saddle to scission. At low T_{tr}, the prescission kinetic energy is close to 20 MeV and decreases to about 2.5 MeV at high T_{tr}. Again, we can stress that temperature dependence of the microscopic transport coefficients has a drastic impact on the prescission kinetic energy. In typical trajectories, the local temperature gets values in the range from 0.1 to slightly over 1 MeV. The blue line in Fig. 11 exhibits the result obtained with the microscopic transport coefficients at local temperature, which gives the value of 15.7 MeV. Once again, one should understand that these values are obtained by superposition of many components depending on the local temperature. On the other hand, the red line denotes the result obtained with macroscopic transport coefficients, which is close to 17.1 MeV. These values are very consistent with our common knowledge.

In Fig. 12 we plot the average value $\langle\delta\rangle$ of fragment deformation at the scission point and the Coulomb interaction energy of fission fragments at the moment of scission as function of T_{tr}. The Coulomb interaction energy was calculated by using the center-of-mass distance of the two fragments at scission and the assumption of unchanged, point charge distribution. The resulting Coulomb interaction energy obtained with the local-temperature microscopic calculation (blue horizontal line) is 154.0 MeV. This value is larger by about 3.6 MeV than that for the macroscopic calculation (shown by a red horizontal line).

It is to be noted that the $\langle\delta\rangle$ at scission was calculated as an event average of the δ at scission points. It is interesting that this quantity depends on the T_{tr} in the way represented in the top panel of Fig. 12. Above 0.5 MeV, this quantity has a monotonically decreasing trend toward oblate shape. This is what we expect when a deformable object, dropping off a slope, moves under a strong influence of friction. This gives rise to the increase of the Coulomb kinetic energy at scission due to the resulting compact shapes as T_{tr} increases.

In addition, we notice that in Figs. 11 and 12 there are "bends" at around $T_{tr} = 0.5$ MeV. We have not clarified the origin of such bends, but we presume that they are due to an interplay between the rapidly increasing friction and decreasing mass tensors at low temperatures, especially due to disappearance of pairing at $T \approx 0.5$ MeV.

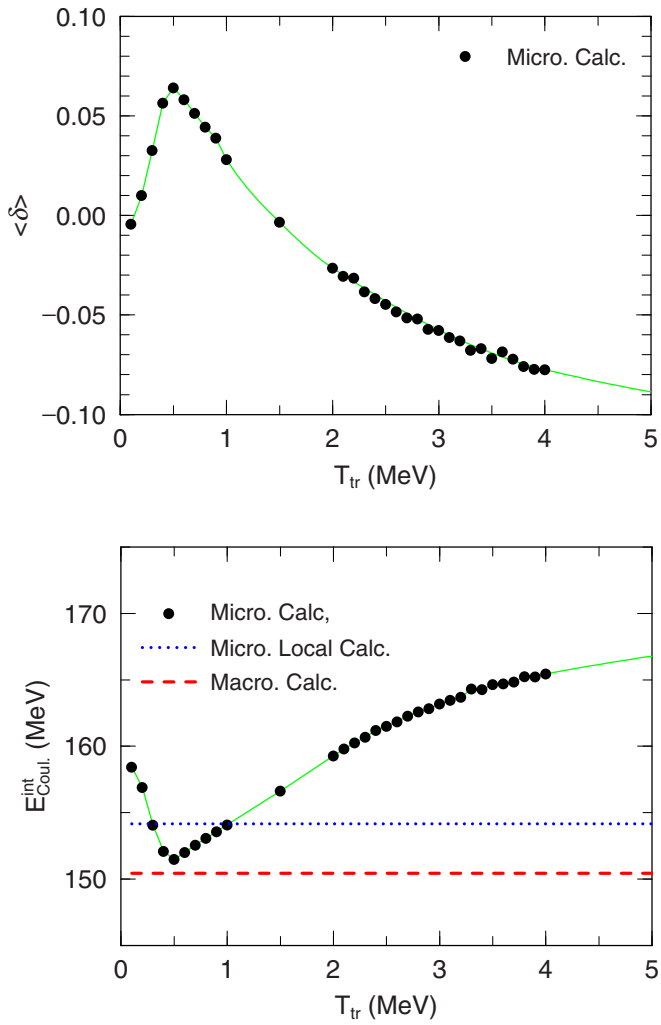

FIG. 12. The average deformation $\langle\delta\rangle$ of fission fragments at scission as function of $T_{\rm tr}$ (top) and the Coulomb interaction energy of fission fragments at scission (bottom) for ^{236}U at $E_x = 20$ MeV.

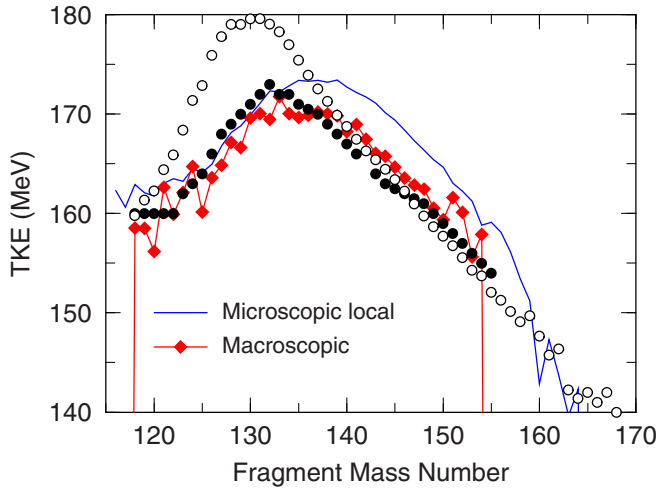

FIG. 13. Comparison of calculated total kinetic energy of fission fragments for ^{236}U with the experimental data of Dyachenkov and Kuzminov [47] (full circles) and Zeynalov *et al.* [48] (open circles) for ^{235}U $+n$.

The total kinetic energy (TKE) defined here as the sum of Coulomb interaction and the prescission kinetic energies is shown in Fig. 13. For comparison, we plot experimental data measured with thermal neutrons [48] and 15.5 MeV neutrons [47]. The total kinetic energy of fragments below $A = 132$ for all calculation follows closely the experimental TKE for 15.5 MeV incident neutrons.

VII. SUMMARY

We have calculated observables for fission of nuclei around ^{236}U at excitation energy of 20 MeV by using the three-dimensional Langevin model and compared them with experimental information. Here, our emphasis was placed on how the microscopic effects in the transport coefficients (inertia and friction tensors) affect various fission quantities. For this purpose, we have carried out calculations with (1) macroscopic transport coefficients which do not depend on local temperature, (2) microscopic transport coefficients calculated at some fixed temperature $T_{\rm tr}$, and (3) microscopic transport coefficients determined at local, deformation-dependent temperature.

We have found that the microscopic friction and mass tensors have strong temperature dependence. Especially, the friction tends to be very small at low temperature. Consequently, it was shown that the mass distributions, prescission kinetic energy, and Coulomb kinetic energy of fragments have strong dependence on the temperature $T_{\rm tr}$ at which the microscopic transport coefficients are calculated. The mass distribution calculated with the microscopic transport coefficients at very low temperature has a peak at the symmetric fission point, indicating the fact that small friction (due to pairing) allows a certain fraction of Langevin trajectories to pass over the ridge between symmetric and asymmetric fission channels and arrive at the valley of macroscopic potential energy. This tendency gets weaker as $T_{\rm tr}$ increases, and eventually even gives rise to a suppression of the symmetric component. When microscopic transport coefficients are calculated at the local temperature, the final outcome of the mass distribution was found to be very similar to that obtained with macroscopic transport coefficients. It was also found that the pairing correction to the potential energy does not affect the mass distribution noticeably even though the paring effect on the friction tensor is significant and alters the mass distribution calculated at different temperatures $T_{\rm tr}$.

The prescission kinetic energy of fission fragments ranges from 25 to 2.5 MeV when $T_{\rm tr}$ is varied from low to high values. Similarly, the average deformation of fragments and Coulomb kinetic energy strongly depend on $T_{\rm tr}$. Therefore, we found again a strong effect of the microscopic transport coefficient depending on $T_{\rm tr}$. When the local temperature is used, however, these quantities tend to give values similar to those calculated with macroscopic transport coefficients in the situation investigated in this work.

We have elucidated the microscopic effect of transport coefficients on Langevin dynamics in this work. However, the calculation is limited to ^{234}U, ^{236}U, and ^{240}Pu at an excitation energy of 20 MeV. More work is necessary if the effects found

in this work apply to other systems including systematic trends of fission observables in nearby nuclei and other regions of excitation energy. As such, they could be the subject of future work.

We are aware that within the Langevin approach one can examine the configuration of system at the scission point. For example, one could find the deformation of light and heavy fragments just before the scission for different values of the mass asymmetry. Such information would be very useful for the approaches based on the scission point model. However, for meaningful results we would have to carry out the calculations with $\delta_1 \neq \delta_2$. Unfortunately, in the present version of the two-center shell model code we use, the microscopic transport coefficients are calculated only for the case $\delta_1 = \delta_2$. The modification to the case $\delta_1 \neq \delta_2$ requires a substantial rearrangement of the whole code. This will take some time. The calculations with $\delta_1 \neq \delta_2$ will therefore be also the subject of our future studies.

ACKNOWLEDGMENTS

The present study includes the results of "Comprehensive study of delayed-neutron yields for accurate evaluation of kinetics of high-burn up reactors" entrusted to Tokyo Institute of Technology by the Ministry of Education, Culture, Sports, Science and Technology of Japan (MEXT). We appreciate informative discussions with Prof. T. Wada (Kansai University) and Prof. Y. Aritomo (Kindai University). Two of the authors, M. D. Usang and F. A. Ivanyuk, would like to express their gratitude to the Laboratory for Advanced Nuclear Energy, Institute of Innovative Research, Tokyo Institute of Technology, for hospitality during their visits to Japan.

[1] P. Fong, Phys. Rev. **102**, 434 (1956).
[2] B. D. Wilkins, E. P. Steinberg, and R. R. Chasman, Phys. Rev. C **14**, 1832 (1976).
[3] J. Randrup and R. Vogt, Phys. Rev. C **80**, 024601 (2009).
[4] R. Vogt, J. Randrup, D. A. Brown, M. A. Descalle, and W. E. Ormand, Phys. Rev. C **85**, 024608 (2012).
[5] K.-H. Schmidt, B. Jurado, C. Amouroux, and C. Schmitt, Nucl. Data Sheets **131**, 107 (2016).
[6] Y. Abe, S. Ayik, P.-G. Reinhard, and E. Suraud, Phys. Rep. **275**, 49 (1996).
[7] P. Fröbrich and I. Gontchar, Phys. Rep. **292**, 131 (1998).
[8] T. Wada, Y. Abe, and N. Carjan, Phys. Rev. Lett. **70**, 3538 (1993).
[9] A. V. Karpov, P. N. Nadtochy, D. V. Vanin, and G. D. Adeev, Phys. Rev. C **63**, 054610 (2001).
[10] T. Asano, T. Wada, M. Ohta, T. Ichikawa, S. Yamaji, and H. Nakahara, J. Nucl. Radiochem. Sci. **5**, 1 (2004).
[11] Y. Aritomo, S. Chiba, and F. Ivanyuk, Phys. Rev. C **90**, 054609 (2014).
[12] Y. Aritomo and S. Chiba, Phys. Rev. C **88**, 044614 (2013).
[13] M. R. Pahlavani and S. M. Mirfathi, Phys. Rev. C **92**, 024622 (2015).
[14] J. Randrup and P. Möller, Phys. Rev. C **88**, 064606 (2013).
[15] A. V. Ignatyuk, K. K. Istekov, and G. N. Smirenkin, Yad. Fiz. **29**, 895 (1979) [Sov. J. Nucl. Phys. **29**, 450 (1979)].
[16] K. T. R. Davies, A. J. Sierk, and J. R. Nix, Phys. Rev. C **13**, 2385 (1976).
[17] R. A. Gherghescu and D. N. Poenaru, Phys. Rev. C **72**, 027602 (2005).
[18] A. J. Sierk and J. R. Nix, Phys. Rev. C **21**, 982 (1980).
[19] J. Blocki, Y. Boneh, J. Nix, J. Randrup, M. Robel, A. Sierk, and W. Swiatecki, Ann. Phys. (NY) **113**, 330 (1978).
[20] M. Brack, J. Damgaard, A. S. Jensen, H. C. Pauli, V. M. Strutinsky, and C. Y. Wong, Rev. Mod. Phys. **44**, 320 (1972).
[21] V. Schneider, J. Maruhn, and W. Greiner, Z. Phys. A: At. Nucl. **323**, 111 (1986).
[22] W. Greiner and J. A. Maruhn, *Nuclear Models* (Springer, Berlin, 1996).
[23] H. J. Krappe and K. Pomorski, *Theory of Nuclear Fission: A Textbook* (Springer, Berlin, 2012), Vol. 838.
[24] H. Hofmann, *The Physics of Warm Nuclei With Analogies to Mesoscopic Systems* (Oxford University Press, New York, 2008).
[25] D. N. Poenaru and R. A. Gherghescu, J. Phys. G: Nucl. Part. Phys. **41**, 125104 (2014).
[26] G. I. Kosenko, F. A. Ivanyuk, and V. V. Pashkevich, J. Nucl. Radiochem. Sci. **3**, 71 (2002).
[27] V. L. Litnevsky, V. V. Pashkevich, G. I. Kosenko, and F. A. Ivanyuk, Phys. Rev. C **89**, 034626 (2014).
[28] G. Adamian, N. Antonenko, S. Ivanova, and W. Scheid, Nucl. Phys. A **646**, 29 (1999).
[29] G. G. Adamian, N. V. Antonenko, and H. Lenske, Phys. Rev. C **91**, 054602 (2015).
[30] H. Hofmann, Phys. Rep. **284**, 137 (1997).
[31] R. Kubo, Rep. Prog. Phys. **29**, 255 (1966).
[32] J. Maruhn and W. Greiner, Z. Phys. **251**, 431 (1972).
[33] S. Suekane, A. Iwamoto, S. Yamaji, and K. Harada, JAERI Memo No. 5918, 1974 (unpublished).
[34] A. Iwamoto, S. Yamaji, S. Suekane, and K. Harada, Prog. Theor. Phys. **55**, 115 (1976).
[35] F. Ivanyuk, S. Chiba, and Y. Aritomo, J. Nucl. Sci. Technol. **53**, 737 (2016).
[36] V. Strutinsky, Nucl. Phys. A **95**, 420 (1967).
[37] V. Strutinsky, Nucl. Phys. A **122**, 1 (1968).
[38] H. J. Krappe, J. R. Nix, and A. J. Sierk, Phys. Rev. C **20**, 992 (1979).
[39] G. D. Adeev, A. V. Karpov, P. N. Nadtochii, and D. V. Vanin, Fiz. Elem. Chastits At. Yadra **36**, 712 (2005) [Phys. Part. Nucl. **36**, 378 (2005)].
[40] W. Swiatecki, Nucl. Phys. A **428**, 199 (1984).
[41] J. R. Nix and A. J. Sierk, Nucl. Phys. A **428**, 161 (1984).
[42] F. Ivanyuk and H. Hofmann, Nucl. Phys. A **657**, 19 (1999).
[43] F. A. Ivanyuk, in *Proceedings of the International Conference on Nuclear Physics "Nuclear Shells - 50 Years"*, edited by Y. Oganessian and R. Kalpakchieva (World Scientific, Singapore, 2000), pp. 456–465.
[44] S. Yamaji, H. Hofmann, and R. Samhammer, Nucl. Phys. A **475**, 487 (1987).

[45] F. A. Ivanyuk, S. Chiba, and Y. Aritomo, Phys. Rev. C **90**, 054607 (2014).

[46] K. Shibata, O. Iwamoto, T. Nakagawa, N. Iwamoto, A. Ichihara, S. Kunieda, S. Chiba, K. Furutaka, N. Otuka, T. Ohasawa, T. Murata, H. Matsunobu, A. Zukeran, S. Kamada, and J.-i. Katakura, J. Nucl. Sci. Technol. **48**, 1 (2011).

[47] P. P. Dyachenko and B. D. Kuzminov, Yad. Fiz. **7**, 36 (1968) [Sov. J. Nucl. Phys. **7**, 27 (1968)].

[48] S. Zeynalov, V. Furman, F.-J. Hambsch, M. Florec, V. Konovalov, V. Khryachkov, and Y. Zamyatnin, in *13th International Seminar on Interaction of Neutrons with Nuclei (ISINN-13)* (Joint Institute for Nuclear Research, Dubna, Russia, 2005), p. 351.